Visualizing dissipative charge-carrier dynamics at the nanoscale with superconducting-charge-qubit microscopy

Berthold Jäck[*]

Princeton University, Joseph Henry Laboratory at the Department of Physics, Princeton, New Jersey 08544, USA

The investigation of novel electronic phases in low-dimensional quantum materials demands for the concurrent development of new measurement techniques that combine surface sensitivity with high spatial resolution and high measurement accuracy. We propose a quantum sensing imaging modality based on superconducting charge qubits to study dissipative charge-carrier dynamics with nanometer spatial and better than nanosecond temporal resolution. Using analytical and numerical calculations, we show that superconducting-charge-qubit microscopy (SCQM) has the potential to resolve temperature and resistivity changes in a sample as small as $\Delta T \leqslant 0.1$ mK and $\Delta \rho \leqslant 1 \times 10^4$ Ω cm, respectively. Among other applications, SCQM will be especially suited to study the microscopic mechanisms underlying interaction driven quantum phase transitions, to investigate the boundary modes found in novel topological insulators and, more broadly, to visualize dissipative charge-carrier dynamics occurring in mesoscopic and nanoscale devices.

I. INTRODUCTION

Topologically protected boundary modes in higher order topological insulators [1,2] and correlated electronic states in magic angle twisted bilayer graphene [3,4] represent only two recent examples of novel quantum phases of matter, which promise new insights into questions of topological matter and many-body physics and which carry the prospect of potential technological applications such as dissipation-less electronic charge transport, spintronic devices, and topological quantum computation.

To date, insights on these quantum materials are derived from transport experiments that measure a global resistance drop across a device, or from other experimental techniques, such as photoelectron spectroscopy or scanning tunneling microscopy, which can map out the equilibrium electronic density of states. All these measurements are however inherently insensitive to charge-carrier dynamics at small length scales, which dictate the global material properties. Therefore the exploration of quantum materials will be accelerated by the concurrent development of new measurement techniques with the ability to measure such local properties with high sensitivity and high spatial resolution.

Quantum sensing microscopy probes, which harness the sensitivity of a two-level quantum system to perturbing fields from the environment, have started to fill out this gap recently [5]. Scanning NV center microscopy [6–8] has proven

especially versatile to study the temperature and conductivity of samples with nanometer spatial resolution [9,10]. Scanning SQUID on tip thermometry (tSOT) [11], as a related technique, offers nanoscale imaging of energy dissipation with unprecedented thermal resolution in devices made from 2D materials [12]. In addition, Microwave impedance microscopy (MIM) [13] emerged as a valuable tool study local resistivity and helped to visualize topological edge states on the perimeter of an insulating bulk [14]. However, the low-temperature operation of these techniques is often limited by technical constraints to temperatures above 1 K, contesting their applicability for the investigation of new quantum phases of matter at lowest temperatures.

II. SCANNING-CHARGE-QUBIT MICROSCOPY

Inspired by these advances, we here propose scanning-charge-qubit microscopy (SCQM) as a new quantum sensing imaging modality to study dissipative charge-carrier dynamics with estimated nanometer spatial and picosecond temporal resolution at temperatures below 1 K, inaccessible to existing techniques. SCQM is based on superconducting charge qubits (CQ), such as the Cooper pair box [15], which are inherently sensitive to charge noise $\delta n(t)$ in the immediate environment [16–18]. This high sensitivity to $\delta n(t)$, limiting the CQ's coherence time to about a microsecond [19,20], renders this type of superconducting qubit less suitable for quantum computation, but on the other hand, makes it a promising candidate for quantum sensing applications, in which $\delta n(t)$ acting on the CQ can serve as a valuable spectroscopic tool.

The noise spectroscopy concept we here describe is based on the physical phenomenon that the equilibrium stochastic motion of charge carriers in conducting materials of resistance R gives rise to Johnson-Nyquist voltage noise $\delta V(t)$. At finite temperature, T, and in the limit of low-frequencies, $k_B T \gg$

---

[*]berthold.jack@alumni.epfl.ch
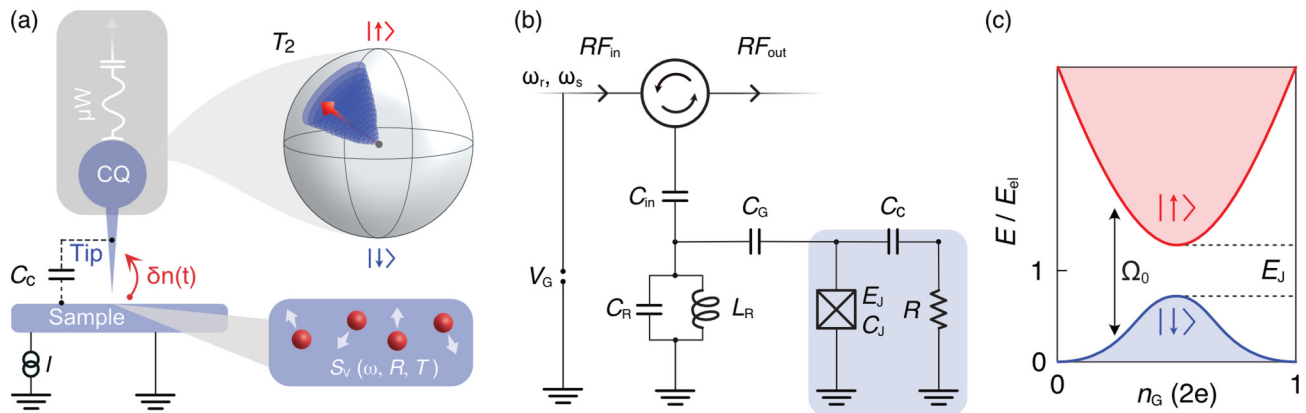
FIG. 1. SCQM: sensing decoherence with superconducting charge qubits. (a) Concept sketch of SCQM that uses a superconducting charge qubit, CQ, to sense voltage fluctuations described by a power spectral density $S_V(\omega, R, T)$ in a sample of interest. The voltage fluctuations are converted into charge fluctuations, $\delta n_G(t)$, by means of a coupling capacitance C_C. $\delta n_G(t)$ induces qubit decoherence, characterized by the dephasing time T_2, and which can be measured via microwave (μW) techniques. Local probe capabilities are realized using a tip, which is galvanically coupled to the qubit and defines a local geometric coupling capacitance, C_C, to the sample. The setup allows for (non)equilibrium measurements of dissipative transport characteristics using either a grounded sample or by applying a current bias I, to the sample. (b) Electrical circuit diagram: SCQM is centered around a Josephson junction (E_J, C_J), which is capacitively coupled (C_G) to a coplanar microwave strip-line resonator CPS, characterized by its capacitance C_R, and inductance L_R. The gate charge n_G can be adjusted through the gate voltage V_G. The capacitively coupled sample is represented as an Ohmic resistor R. The CPS is addressed using two-tone spectroscopy, ω_r and ω_s, in a reflective measurement scheme via an input capacitance C_{in}. (c) The charge dispersion of the CQ's two lowest eigenstates is shown as a function of n_G. E_J lifts their degeneracy at $n_G = 0.5$ and induces a level splitting, Ω_0, between $|\uparrow\rangle$ and $|\downarrow\rangle$.

$\hbar\omega$, this type of noise can be characterized by its voltage noise spectral density, $S_V = 4k_B T R$ (k_B is Boltzman's constant, $\hbar$ is Planck's constant) [21,22]. Measuring Johnson noise in or out of equilibrium, e.g., in the absence or presence of an external drive current, I, giving rise to the dissipative motion of charge carriers, allows to characterize a sample's resistance, and to quantify the underlying charge-carrier dynamics by tracking temperature changes through scattering-induced energy dissipation [Fig. 1(a)]. In addition, such measurements can also help to distinguish between different transport regimes, such as the diffusive and ballistic motion of charge carriers [23].

Dissipative transport characteristics in a sample can be probed using a CQ with the help of a coupling capacitance C_C [Fig. 1(a)]. The capacitance serves as a mediator, effectively converting voltage fluctuations, $\delta V(t)$, in the sample into charge noise on the qubit. For sufficiently large C_C values, voltage fluctuations can therefore induce decoherence of a prepared CQ state. Decoherence of the CQ (and generally any two-level quantum system) resulting from that interaction can be quantified my measuring its decoherence time, T_2. T_2 can, therefore, be used as a measurable quantity to probe dissipative processes in the immediate qubit environment, e.g., by realizing a microwave read-out of the qubit state in a circuit quantum-electrodynamics (cQED) setup [24]. Importantly, a cQED realization with GHz bandwidth also lends itself to time-resolved studies using a pulsed measurement scheme, which could facilitate the investigation of dissipative transport dynamics under nonequilibrium conditions with, in principal, picosecond temporal resolution [25].

Realizing this noise spectroscopy concept in a local probe scenario requires a geometric coupling capacitance, the lateral extent of which is small enough to investigate dissipative charge-carrier dynamics spatially resolved. Unlike in scanning NV microscopy, where the pointlike NV quantum sensor

brought in the vicinity of a sample facilitates a spatial resolution on the order of 10 nm [6–8], superconducting charge qubits are typically as large as tens of micrometers [24]. Achieving spatial resolution, therefore, demands for a suitable coupling concept to the qubit's charge degree of freedom. Following other scanning probe techniques, we propose to use thin tips made from superconducting wire (diameter $\leqslant 5$ μm), to realize a local geometric coupling capacitance to a sample surface underneath on the order of femtofarads [see Fig. 1(a)] [26]. In this scheme we propose, the wire itself is attached and galvanically coupled to one of the CQ capacitor pads. Employing the geometric capacitance of a thin tip is key to our proposal and overcomes the existing spatial resolution limit of superconducting qubits for the application as local quantum sensors [27].

III. DECOHERENCE IN A CHARGE QUBIT

In the most simple implementation, the CQ corresponds to a charge island formed between a Josephson junction, characterized by the coupling energy E_J and its capacitance C_J, and a gate capacitance C_G, which allows to adjust the island charge, $n_G = C_G V_G / 2e$, in units of Cooper pairs through applying a gate voltage, V_G (e is elementary charge) [Fig. 1(b)] [28]. In the limit of the charging energy, $E_C = e^2 / 2C_\Sigma$, exceeding the Josephson coupling energy $E_C \gg E_J$, the system can be reduced to the two lowest charge states of the island $|\uparrow\rangle$ and $|\downarrow\rangle$, respectively. E_C is determined by the total capacitance to ground, $C_\Sigma = C_J + C_G$, and possible other contributions such as the coupling capacitance C_C. In this case, the effective Hamiltonian can be rewritten in the form of a fictitious spin-1/2 particle, $H = -E_{el}/2\sigma_z - E_J/2\sigma_x$, under the influence of the pseudomagnetic fields $B_z = E_{el}$ and $B_x = E_J$ with the electrostatic energy $E_{el} = 4E_C(1 - 2n_G)$ [29]. The charge

dispersion of H [Fig. 1(c)] illustrates the role of E_J as a symmetry breaking term that lifts the degeneracy of $|\uparrow\rangle$ and $|\downarrow\rangle$ states at $n_G = 0.5$. This results in a gapped excitation spectrum with the level splitting $\Omega_0 = \sqrt{E_{el}^2 + E_J^2}$. For a given gate charge, the CQ, therefore, corresponds to a two level quantum system, the coherent superposition of which can be mapped onto a Bloch sphere [cf. Fig. 1(a)].

Interaction with a dissipative environment can lead to decoherence and relaxation of a prepared CQ state. The strength of this process is determined by the CQ properties and the coupling strength between the CQ and the environment. Voltage noise, $\delta V(t)$, present in the environment is converted to charge noise, $\delta n_G(t)$, through C_C [cf. Fig. 1(a)]. In the limit $E_C \gg E_J$, this process can be rationalized conveniently and will, in first order, only result in longitudinal charge fluctuations ($\delta n_G(t) \| \sigma_z$), which can be rationalized in terms of a coupling Hamiltonian $H_C(t) = 8E_C \sigma_z \delta n_G(t)$ [30]. Under the influence of this noise term, the prepared quantum superposition of a CQ state will experience dephasing described by $\Delta\phi = \int_{-\infty}^{\infty} dt H_C(t)$ [31].

On this basis, we quantify the dephasing of a CQ state induced by Johnson noise in the environment characterized by an Ohmic resistor R [cf. Fig. 1(b)]. The magnitude of the resulting charge noise spectral density, $S_n = \zeta(\omega)S_V$, is determined by the transfer function, $\zeta = (\eta C_C/2e)^2$, which we can assume to be frequency-independent in the limit $\hbar\omega \ll k_B T$. The scaling factor, $\eta = C_C/C_\Sigma$, renormalizes C_C to an effective value with respect to the total capacitance to ground, C_Σ. Evaluating the dephasing, $\Delta\phi$, in terms of the phase-phase correlation function in the low frequency limit [31], one can evaluate the dissipation induced dephasing time, T_{2M}, as

$$1/T_{2M} = 8\pi^2 (k_B T/\hbar)\epsilon\eta^2 \qquad (1)$$

with $\epsilon = R/R_Q$ as the normalized resistance (R_Q is Klitzing's constant), Appendix A. Measuring the CQ dephasing characteristics therefore allows to directly determine R and T of a capacitively coupled sample. It bears noting that the response of the dephasing constant, $2\pi\nu_M = 1/T_{2M}$, with respect to these parameters, $\partial\nu_M/\partial(\epsilon T) = 4\pi (k_B/\hbar)\eta^2$, is constant, rendering the CQ an ideal quantum sensor with linear output characteristics.

IV. MICROWAVE CONTROL AND READ-OUT OF A CQ

The qubit state and its dephasing characteristics can be interrogated using microwave photons in a cQED architecture [24,29]. In the example shown in Fig. 2(a), the qubit is capacitively coupled to a superconducting coplanar stripline resonator (CPS) of bare frequency ω_r, realizing a reflective read-out scheme [cf. Fig. 1(b)]. At strong coupling, $g \gg \kappa, \gamma$, in which the resonator-qubit coupling g, exceeds both the inverse cavity and the qubit lifetime, κ and γ, respectively the CQ states ($|\uparrow\rangle$ and $|\downarrow\rangle$) are entangled with the resonator photon number states $|n\rangle$. In the dispersive limit, $\omega_r \gg \Omega_0$, it is possible to probe the CQ state by measuring the phase shift, $\phi = \pm \tan^{-1}(2g^2)/(\kappa\Delta)$, of the reflected microwave tone ω_r [29].

Applying an additional spectroscopy tone, ω_s, to the CPS allows to prepare and probe an arbitrary coherent superposition of the $|\uparrow\rangle$ and $|\downarrow\rangle$ state. Importantly, such
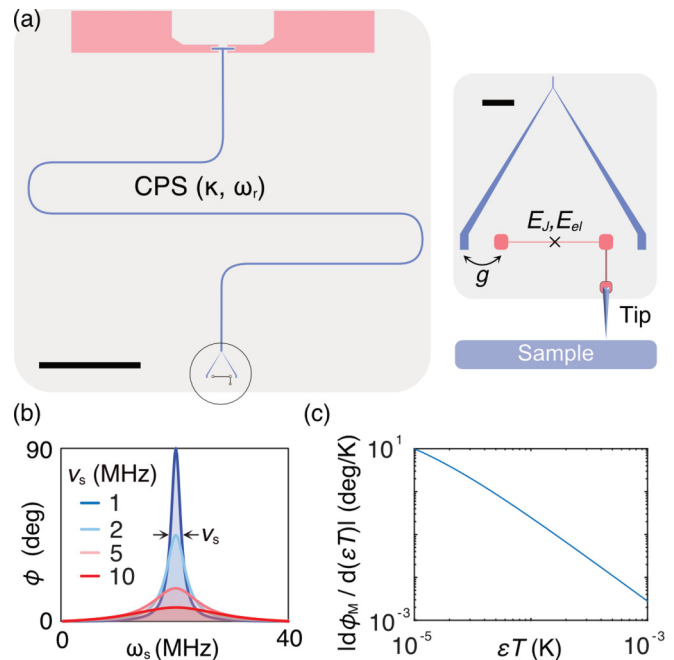
FIG. 2. Microwave read-out of CQ decoherence (a) Drawing of a resonator charge qubit implementation for SCQM. The red patches are the launchers for coupling to the circuitry, the coplanar strip-line resonator (CPS) (blue) is characterized by its photon decay rate κ and its resonance frequency ω_r (scale bar 800 μm). (Inset) The CPS couples to the qubit, characterized by E_J and E_{el}, through capacitive couplers (red pads) with strength g. The tip is galvanically coupled to one of the capacitance pads (scale bar 50 μm). (b) Calculated homodyne phase shift, ϕ, of the cavity tone as a function of the applied spectroscopy tone, ω_s, for different indicated linewidths ν_s. (c) Calculated change of the phase shift peak maximum ϕ_M in (b) with respect to changes in ϵ and T.

two-tone spectroscopy yields a strong (no) phase shift of the reflected microwave signal in a homodyne detection scheme, when ω_s is on (off) resonance with the qubit transition. This is illustrated in Fig. 2(b), which shows a calculated spectroscopy tone sweep across the $|\uparrow\rangle$-$|\downarrow\rangle$ transition. Hence, such two-tone spectroscopy is suited to both control and read-out the state of a CQ in our quantum sensing scheme.

Most commonly, pulse sequence experiments, such as Ramsey fringe or spin-echo, are used to measure T_2 with high accuracy [5]. Observing the quantum state evolution at different pulse delays in these experiments typically requires long measurement times on the order of minutes to hours. In the context of SCQM, this approach appears less suited from a practical perspective, as mapping out T_2 on a 256 × 256 point grid on a sample surface would result in measurement times on the order of a day or more.

V. FAST READ-OUT OF CQ DECOHERENCE

We here propose an alternative approach for determining the dephasing characteristics that lends itself to fast measurement schemes and is key to this proposal. It is based on a line shape analysis of the spectroscopy tone sweep shown in Fig. 2(b), facilitating the direct determination of the CQ's T_2. In the low power limit, $n_S \to 0$, in which only
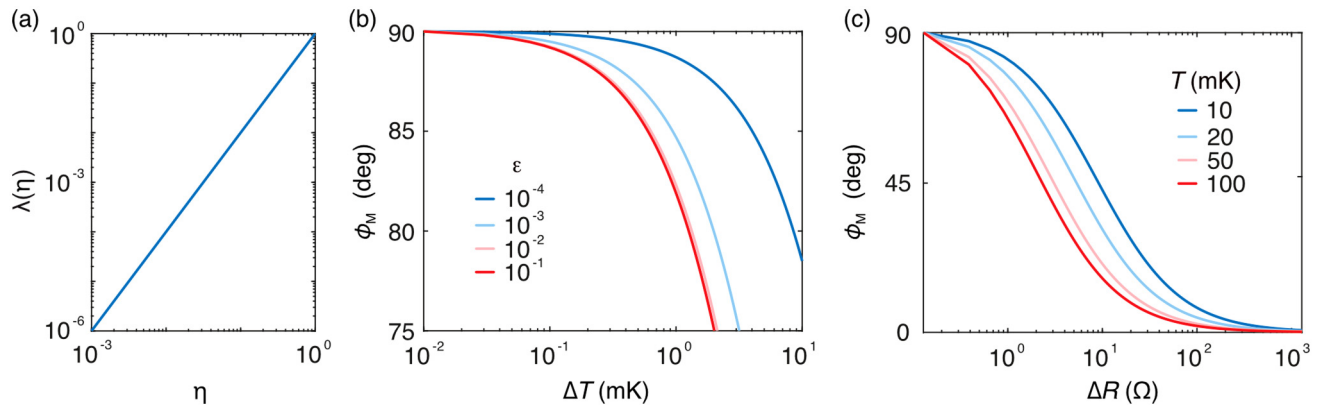
FIG. 3. Response the SCQM quantum sensor. (a) Normalized calculated response of the CQ quantum sensor, $\lambda = \partial \phi_{\mathrm{M}} / \partial (\epsilon T)$, to changes in ϵ and T as a function of η. Shown is the calculated change of ϕ_{M}. (b) Calculated homodyne phase shift, ϕ_{M}, as a function of ΔT, in a capacitively coupled sample ($\eta = 0.1$, $\nu_\phi = 320$ kHz) at different indicated values of ϵ. (c) ϕ_{M}, as a function of ΔR, in a capacitively coupled sample ($\eta = 0.1$, $\nu_\phi = 320$ MHz) at different indicated T values.

few spectroscopy photons, n_{S}, are occupying the resonator, the line shape of the phase peak can be approximated by a Lorentzian function, $\phi(\omega_{\mathrm{s}}, \nu_{\mathrm{s}})$, the half-width half-maximum of which, ν_{s}, is directly linked to T_2 through $2\pi \nu_{\mathrm{s}} = 1/T_2$ [20]. Crucially, owing to its Lorentzian nature, the maximum (minimum) of the phase peak (dip) is directly proportional T_2, $\phi_{\mathrm{M}} = 1/(\pi \nu_{\mathrm{s}}) = 2 T_2$. Hence, T_2 can be determined by measuring ϕ_{M} at a fixed ω_{s}, set to be on resonance with the CQ transition Ω_0. We point out that the reciprocal dependence of $\phi_{\mathrm{M}} \propto (\epsilon T)^{-1}$ on ϵ and T, renders this detection scheme highly responsive to even smallest changes in these quantities, as illustrated in Fig. 2(c). Overall, this proposed detection scheme realizes a fast read out of the qubit decoherence characteristics, and it should facilitate the imaging of local dissipative charge-carrier dynamics on a sample surface in a realistic experimental time frame. Nonetheless, Ramsey fringe and spin-echo experiments will be indispensable to calibrate and verify the described lineshape analysis, and to determine the CQ's intrinsic dephasing rate with high accuracy.

VI. COUPLING CAPACITANCE AND SPATIAL RESOLUTION

The ability of SCQM to measure dissipative transport dynamics in a capacitively coupled sample depends on the intrinsic CQ properties, the SCQM device architecture and, in particular, on the specific coupling geometry determining C_{C}. The response λ of the CQ to changes in the sample's temperature and resistivity, $\lambda = \partial \nu_{\mathrm{M}} / \partial (\epsilon T) \propto \eta^2$, can be significantly enhanced by maximizing C_{C} and, at the same time, by minimizing C_Σ, such that $\eta \to 1$. Figure 3(a) illustrates that enhancing η by one order of magnitude already increases λ by two orders of magnitude. We have performed electrostatic simulations of the resonator-CQ-tip-sample geometry [Fig. 2(a)] with the goal of minimizing C_Σ and obtaining a realistic estimate for η, Appendix B. Our results show that an optimized CPS design yields $C_\Sigma < 3$ fF. At the same time, large CQ resonator coupling values, $g \gg 100$ MHz, required for the dispersive readout scheme, $g \gg \kappa, \gamma$ can be maintained. We note that our simulation results on the capacitance values are comparable to previously reported experimental values for Cooper pair boxes [20]. Overall, key CPS design

aspect, which we found from our simulations, is to minimize the surface area of the capacitor pads that couple the Josephson junction to the resonator [Fig. 2(a) inset].

Concerning the realization of sufficiently large C_{C} values, one has to find the right balance between, on the one hand maximizing the C_{C} for obtaining a high λ and, on the other hand, maintaining a high spatial resolution, Δx. Using a thin conical wire of base diameter 5 μm as a tip attached to one of the capacitor pads [see Fig. 2(a) inset], our analytical calculations show that $\eta \approx 0.1$ and $\Delta x \geqslant 100$ nm can be achieved, Appendix C. In this case, Δx is limited by the geometrically distributed stray capacitance of the tip wire. Using a thin superconducting nanowire with a diameter of 50 nm as an alternative still allows to reach values of $\eta > 0.01$ but with a much enhanced $\Delta x \leqslant 50$ nm, Appendix C. Ultimately, the tip choice will depend on the respective requirements of an experiment on λ and Δx.

VII. DECOHERENCE MEASUREMENT AND SIGNAL TO NOISE RATIO

Crucially, the detection of dissipative transport induced qubit dephasing requires that its dephasing rate, ν_{M}, exceeds the intrinsic dephasing rate, ν_ϕ, in order to yield a measurable signal in the total dephasing, $1/T_2 = 2\pi \nu_2 = 2\pi (\nu_{\mathrm{M}} + \nu_\phi) = 1/(T_{2\mathrm{M}} + 1/T_\phi) \approx 1/T_{2\mathrm{M}}$, for $\nu_{\mathrm{M}} \gg \nu_\phi$. The ν_ϕ of superconducting CQ has been determined previously, $\nu_\phi \approx 320$ kHz [20], and it was found to be limited by $1/f$-charge noise, which originates from two-level systems (TLS) at the surfaces and interfaces of the constituent materials [16–18]. This value defines the lower bound of the minimal detectable dephasing rate. Additional qubit dephasing, ν_{M}, induced by a finite temperature and/or resistance in the sample of interest, adds to the ν_ϕ, and it will change the total dephasing, $1/T_2 = 2\pi (\nu_{\mathrm{M}} + \nu_\phi)$. These changes in qubit dephasing can be tracked by measuring changes in the Lorentzian amplitude of the homodyne phase, ϕ_{M}.

Based on these considerations we calculate the dependence of ϕ_{M} on changes in temperature, ΔT, and resistance, ΔR [cf. Fig. 2(b)]. To this end, we calculate ϕ_{M} as a function of ΔT and ΔR. Figure 3(b) displays $\phi_{\mathrm{M}}(\Delta T)$ for different values of ϵ, and illustrates the high sensitivity of the CQ

to even smallest ΔT. Using realistic setup parameters (see caption), our calculations reveal that a temperature change of $\Delta T = 1$ mK, such as that induced by dissipative charge-carrier dynamics in a sample, already reduces $\Delta \phi_M \approx 10\%$. The $\phi_M(\Delta R)$, shown in Fig. 3(c), displays similar sensitive characteristics—a change of $\Delta R = 10\ \Omega$ results in $\Delta \phi_M \approx 50\%$. The bare value, $\phi_M \to 90°$, for $(\Delta T, \Delta R) \to 0$, represents the Lorentzian amplitude at a given ν_ϕ.

The signal-to-noise ratio (SNR) and the attainable sensitivity of SCQM to temperature and resistance changes are determined by the noise level of the amplification line for the microwave signal. Its noise is commonly dominated by the number of thermal photons, $n_D = k_B T_D / (\hbar \omega_r)$, generated in the high-electron-mobility amplifier (HEMT) used to amplify the microwave signal at cryogenic temperatures ($T_D = 4$ K). A conservative estimate of that number for our concept yields $n_D \approx 100$. In a homodyne detection scheme at $g^2/(\kappa \Delta) \gg 1$, we define SNR $= \sqrt{m}(n_P/n_D)$, where m corresponds to the number of measurements and $n_P = n\kappa \tau/2$ to the number of collected photons during a finite integration period τ.

Given a cavity enhanced CQ lifetime of $1/\gamma = (\Delta/g)^2 \kappa^{-1} \approx 100\ \mu$s and a low power read-out, $n \leqslant 10$, we calculate an upper bound SNR $= 5\sqrt{m}$, for $\tau = 1/\gamma$. Considering the experimentally determined CQ lifetime of superconducting charge qubits, $1/\gamma \approx 2\ \mu$s [20], we obtain a realistic estimate SNR $= 10^{-1} \cdot \sqrt{m}$. Hence, with a sufficient amount of averaging, $(m > 10^6)$, SNR > 100 can be realized, which should facilitate a temperature and resistance resolution of $\Delta T \leqslant 0.1$ mK and $\Delta R \leqslant 0.1\ \Omega$, respectively [cf. Figs. 3(b) and 3(c)]. Assuming a tip diameter of 50 nm, a change in resistivity of $\Delta \rho \leqslant 1 \times 10^4\ \Omega$ cm could be resolved.

Fast scanning operation of SCQM, on the other hand (256×256 grid, total measurement time $t < 30$ min), can be realized with moderate averaging ($m = 10^4$). This results in SNR $= 10$, which would still allow to detect $\Delta T \approx 1$ mK and $\Delta \rho \leqslant 5 \times 10^4\ \Omega$ cm. If an even higher SNR is required, using Josephson parametric amplifiers instead of HEMTs could enhance the SNR and, at the same time, reduce the measurement time by up to two orders of magnitude [32].

VIII. TECHNICAL ASPECTS: CHARGE QUBIT

SCQM is designed around established fabrication and measurement techniques for qubits and off-the-shelve technology for the scanning module and cryostat environment. In particular, the design and fabrication of superconducting qubits has experienced a tremendous development [33], promising an optimized performance beyond previously reported Cooper pair box results of $1/\gamma \leqslant 1\ \mu$s [20], even in the more complex environment of a SCQM setup. Enhanced qubit performance could be, first, achieved by optimizing the constituent materials and fabrication processes [34–36]. This could reduce the TLS density, which results in a reduction of ν_ϕ and an enhancement of the SNR. Second, the CQ's performance as a sensor could be enhanced by tuning the E_J/E_C ratio to larger values [37]. Model calculations at $n_G = 0.25$ and for $E_J/E_C \leqslant 1$ reveal an optimum ratio at $E_J/E_C = 1$. At this ratio, the reduction in the qubit response ($\propto E_C^2/E_J$), owing to a larger E_J, would be balanced out by an increased SNR through

the increased qubit lifetime, $1/\gamma \propto E_J/E_C^2$ [38]. The corresponding intrinsic dephasing time ($n_G = 0.25$, $C_\Sigma = 2.5$ fF) can be approximated to $T_\phi \approx 250$ ns [38]. It bears noting that biasing the charge qubit to the sweet spot, $n_G = 0.5$, where the largest intrinsic dephasing time, $T_\phi \approx 500$ ns has been reported [20], is detrimental to its operation as a quantum sensor. At this bias point, the qubit is only sensitive to second order charge noise, reducing its response considerably [19], and the qubit lifetime reaches its minimum [30], hurting the SNR of the qubit sensor.

Gate charge drift is a known weak spot of superconducting qubits with charge degrees of freedom, and it results in fluctuations of the gate charge bias point on the time scale of minutes [39]. This effect can be compensated for by implementing a suitable feedback mechanism for n_G. In the context of SCQM, a viable concept can capitalize on the comparably short time required to record an individual pixel of a decoherence map (≈ 1 ms), which is facilitated by the proposed fast read-out scheme. Hence, during the measurement of a decoherence map and after a given measurement time has passed, one could include periodic recalibration steps for n_G. Those steps would simply involve a n_G-dependent spectroscopy in which ω_s is fixed to the level splitting at the desired n_G bias point.

Moreover, low loss CPS resonators with internal quality factors $Q_i > 10^5$ in the limit $n_s \to 0$ can be reliably fabricated from different materials today [40]. These advances should help to satisfy $g > \kappa$ in the more complex environment of a SCQM setup ($\kappa = \omega_r/Q_i$). Potential Purcell losses into the DC lines, which connect to the sample, via C_C can be mitigated by appropriate on- and off-chip filtering [41].

IX. TECHNICAL ASPECTS: SCANNING OPERATION.

Previous studies, some of them based on commercially available components, already demonstrated the feasibility of integrating scanning probe experiments into dilution refrigerator cryostats, while maintaining lowest mechanical vibrations and lowest electron temperatures [27,42,43], an aspect crucial to the operation of the CQ sensor. Yet, attention has to be paid to a proper thermalization and filtering of the DC lines needed for the scanning and device operation [43–45].

Finally, regarding the tip-to-qubit fabrication, a tip wire could be fused to a capacitor pad by means of focused ion beam assisted deposition under suitable grounding and thermalization conditions, an approach commonly practiced to fabricate scanning NV tips [46]. Microfabricated probe tips could present an attractive alternative, and they have been already successfully employed in scanning tunneling microscopy applications [47]. In this all-on-chip concept, the tip could be fabricated alongside the resonator qubit structure in the same deposition/etching processes, potentially reducing the overall complexity of the fabrication process and eliminating the introduction of new materials loss channels. In this regard, a technically comparable scanning microwave resonator microscopy, which uses a coplanar waveguide structure on a planar chip with microfabricated tips, has already been implemented [48]. This work also demonstrated the compatibility of on-chip sensors with AFM qPlus sensor

TABLE I. Scanning probe techniques for studying dissipative charge-carrier transport. Comparison between quantum sensing and related measurement techniques, which probe dissipative charge-carrier dynamics with spatial, Δx, and temporal, $\Delta \tau$, resolution over a temperature range. The relevant measurement quantities are listed.

Technique	Temperature range (K)	Quantities (Resolution)	Δx	$\Delta \tau$
Scanning NV [10]	4–300	σ (1×10^{-4} Ω^{-1} cm^{-1}) T ($\leqslant 5$ mK)	40 nm	ps [25]
tSOT [11,12]	0.3–10	T ($\leqslant 1$ μK)	>50 nm	–
MIM [13]	2–300	ρ	100 nm	–
SCQM	$\leqslant 0.1$	ρ ($\leqslant 1 \times 10^{4}$ Ω cm) T ($\leqslant 0.1$ mK)	$\leqslant 50$ nm	<100 ps [25,50]

technology [49] for enhanced microscopy performance. We, therefore, conclude that SCQM should be realizable based on the current state of technology.

X. SCIENTIFIC USE CASES FOR SCQM

To discuss the perspectives of SCQM in the context of quantum materials, it is instructive to review the current state of related measurement techniques. Table I contrasts the capabilities of some existing microscopy techniques to probe dissipative charge-carrier transport with the estimated performance of SCQM. Among those techniques, scanning NV microscopy represents the most versatile tool with demonstrated capabilities of tracking electrical conductivity and temperature changes with nanometer spatial, Δx, and, in principal, picosecond temporal, $\Delta \tau$, resolution across a large temperature range down to 4 K [10]. Thermal imaging with tSOT operating at $T \geqslant 300$ mK, offers DC thermal imaging capabilities with an unprecedented temperature resolution of $\Delta T \leqslant 1$ μK and $\Delta x \approx 100$ nm [11,12]. MIM is specialized on resistivity imaging with $\Delta x \approx 100$ nm at $T > 2$ K [13]. In comparison, SCQM offers resistivity and temperature imaging with an estimated $\Delta x \leqslant 50$ nm and $\Delta \tau < 100$ ps, the latter of which is only limited by the gate time of the qubit charge state [25,50]. Hence, it has potential capabilities similar to those of scanning NV microscopy, but operates in a lower temperature window much below 1 K.

Put in the context of quantum materials, SCQM will be especially suited for a number of different applications. It could provide microscopic insight on interaction driven quantum phase transitions occurring at temperatures at or below 1 K. Examples would be the superconductor-insulator-transition observed in magic angle twisted bilayer Graphene [3,4] and in monolayer WTe$_2$ [51,52]. Through its potential to distinguish between different transport regimes, SCQM should also be of value to detect and study the transport characteristics of topologically protected boundary states in novel higher order topological insulator platforms [1,53], and to shed light on hydrodynamic transport and the underlying mechanisms, too [54–56]. In this context, dynamic decoupling pulse sequences [5] could be used to determine the full frequency-dependent spectrum of the noise spectral function, $S_V(\omega, T, R)$, potentially disclosing further information about the underlying microscopic processes. Owing to the potential high temporal resolution $\delta \tau < 100$ ps [50], SCQM could also facilitate the investigation of charge-carrier dynamics

in a variety of mesoscopic and nanoscale devices, such as the nonequilibrium quasiparticles in superconducting films, which are known to deteriorate the performance of superconducting qubits [57,58]. More broadly, the noise spectroscopy concept based on qubit decoherence described above could also be realized in nonlocal experiments using pure on-chip realizations (cf. Ref. [23]).

XI. CONCLUSION

We proposed SCQM as a new quantum sensing imaging modality to study dissipative charge-carrier dynamics in low-dimensional quantum materials. Backed up by model calculations, we demonstrate design concepts for local probe realizations based on the geometric capacitance forming between a sample and a tip, which is coupled to the superconducting charge qubit. We propose a tangible scheme for fast microwave read out of the qubit decoherence using standard homodyne techniques, facilitating fast scanning operation and realistic measurement times. Our analytical and numerical analyses reveal the potential capability of SCQM to resolve temperature and resistivity changes of a sample as small as $\Delta T \leqslant 0.1$ mK and $\Delta \rho \leqslant 1 \times 10^{4}$ Ω cm, respectively. SCQM overcomes existing limitations of superconducting qubits for quantum sensing microscopy applications, and will be especially suited to study interaction driven quantum phase transitions in low-dimensional phases of matter, visualize the local transport characteristics of novel topological materials as well as to investigate dissipative charge-carrier dynamics in mesoscopic and nanoscale devices with high spatial and high temporal resolution.
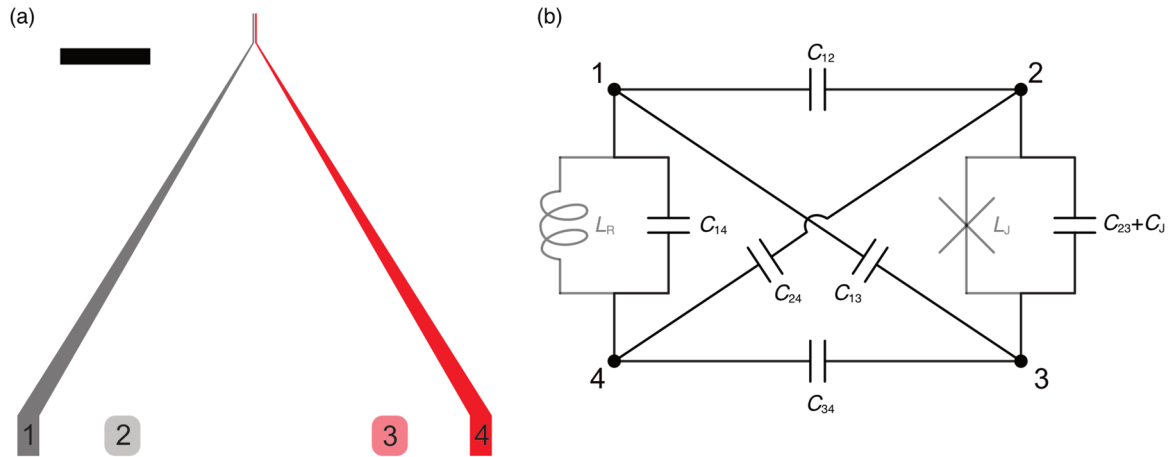
FIG. 4. Electrostatic simulation of qubit-resonator capacitance. (a) Shown is the geometry used to simulate the capacitance values between the resonator (1, 2) and qubit (3, 4) pads (scale bar 50 μm). (b) Corresponding circuit diagram used to derive the total total capacitance to ground, C_Σ, in Eq. (B2) by means of a theory of nodes analysis. The capacitance C_{14} between node 1 and 4 corresponds to the coplanar stripline resonator (CPS) capacitance C_R (L_R is the CPS inductance). The total capacitance between node 2 and 3 is the sum of C_{23} and the Josephson junction capacitance, C_J (L_J is the Josephson inductance).

APPENDIX A: DECOHERENCE OF A SUPERCONDUCTING CHARGE QUBIT COUPLED TO A DISSIPATIVE ENVIRONMENT

The time-dependent dephasing, $\Delta\phi(t) = \int_{-\infty}^{\infty} dt H_C(t)$, of a prepared quantum state of a superconducting charge qubit, CQ, subjected to gate charge noise, $\delta n_G(t)$, can be quantified in terms of a dephasing factor, $f(t) = \exp(\langle\Delta\phi(t)\rangle^2)$. $f(t)$ can be analytically evaluated by means of the phase-phase correlation function [31],

$$f(t) = \exp\left[-\frac{1}{2}\left(\frac{t}{\hbar}\right)^2\left(\frac{\partial H}{\partial n_G}\right)^2 \right.$$
$$\left. \times \int_{-\infty}^{\infty} d\omega\, \zeta(\omega)S_V(\omega)\,\text{sinc}^2\left(\frac{\omega t}{2}\right)\right], \quad \text{(A1)}$$

where $\hbar$ denotes Planck's constant and ω the frequency. In the limit $E_C \gg E_J$, in which the Coulomb energy, E_C, strongly exceeds the Josephson coupling energy, E_J, described in the main text, the coupling term simplifies to $\partial H/\partial n_G = 8E_C$ (n_G is a gate charge) [30]. The environmental noise is characterized by its voltage noise spectral density, $S_V(\omega)$, which couples to the qubit through the transfer function, $\zeta(\omega)$.

We are interested in CQ dephasing induced by Johnson noise in the low frequency (classical) limit, $\hbar\omega \ll k_B T$ (k_B is Boltzman's constant, T is a temperature) [21,22], characterized by its dephasing time, T_{2M}. Using the noise power spectral density of Johnson noise, $S_V(\omega \to 0) = 4k_B T R$, and assuming a frequency-independent transfer function, $\zeta = (\eta C_C/2e)^2$, we evaluate Eq. (A1) (R is the resistance of sample, e is the elementary charge), and find

$$f(t) = \exp\left[-\frac{t}{T_{2M}}\right] = \exp\left[-t\, 8\pi^2 \frac{k_B T}{\hbar}\eta^2\epsilon\right]. \quad \text{(A2)}$$

Here, $\eta = C_C/C_\Sigma$ (C_C is the coupling capacitance, C_Σ is the total capacitance to ground) describes the normalized

coupling capacitance and $\epsilon = R/R_Q$ (R_Q is Klitzing's constant) the normalized resistance. From Eq. (A2), we can directly read the dephasing constant ν_M,

$$2\pi\nu_M = \frac{1}{T_{2M}} = 8\pi^2\frac{k_B T}{\hbar}\eta^2\epsilon. \quad \text{(A3)}$$

APPENDIX B: ELECTROSTATIC SIMULATION OF THE QUBIT-RESONATOR CAPACITANCE

The sensitivity of the CQ quantum sensor strongly depends on the coupling strength between the CQ and the capacitively coupled sample. The transfer function of this coupling, $\zeta = (\eta C_C/2e)^2$, is determined by the coupling capacitance, C_C, and by $\eta = C_C/C_\Sigma$, which renormalizes C_C with respect to the total capacitance to ground, C_Σ. Enhancing the sensitivity of the CQ sensor therefore demands maximizing C_C while, at the same time, minimizing C_Σ.

We carried out electrostatic simulations with the goal of minimizing C_Σ. To this end we optimized the resonator-qubit geometry, mostly targeting the size and the spatial arrangement of the capacitor pads and resonator strips. We simulated the capacitance matrix $\mathbf{C}$ of the qubit-resonator structure shown in Fig. 4(a) using Ansys Maxwell (we assumed a realistic metal film thickness of $h = 200$ nm). We obtain

$$\mathbf{C} = \begin{bmatrix} C_{11} & -C_{12} & -C_{13} & -C_{14} \\ & C_{22} & -C_{23} & -C_{24} \\ & & C_{33} & -C_{34} \\ & & & C_{44} \end{bmatrix}$$

$$= \begin{bmatrix} 57.0 & -1.6 & -2.8 & -46.6 \\ & 4.7 & -0.33 & -2.8 \\ & & 4.7 & -1.6 \\ & & & 5.1 \end{bmatrix} \text{fF.} \quad \text{(B1)}$$
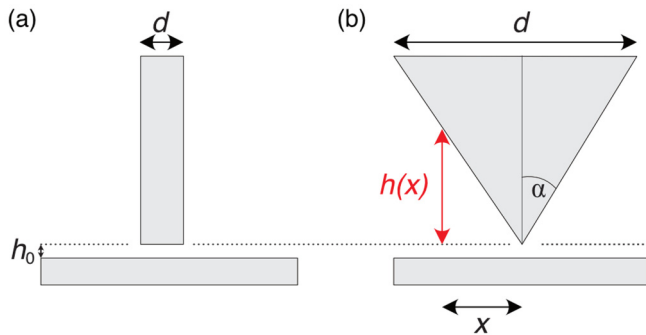
FIG. 5. Tip geometries for SCQM. (a) Nanowire tip, the shape of which can be approximated by a cylinder of diameter d separated from the sample surface by a distance h_0. (b) A metallic wire tip is characterized by a conically shaped tip apex. The apex is defined by its diameter d and its opening angle α.

We derive C_Σ by means of a method of nodes analysis of the corresponding circuit diagram shown in Fig. 4(b). We note that C_{14} corresponds to the coplanar stripline resonator capacitance, C_R [cf. Fig. 1(b)]. Moreover, C_{23} between node 1 and node 3, as well as the corresponding simulated value [cf. Eq. (B1)] do not contain the additional contribution of the Josephson junction capacitance, C_J [cf. Fig. 4(b)]. However, the estimated value of $C_J \ll 1$ fF for typical junction geometries (junction area 100 nm^2, tunnel barrier thickness 1 nm) can be neglected, $C_J \ll C_{23}$. Finally, we arrive at

$$C_\Sigma = \frac{C_{23} + (C_{12} + C_{24}) \cdot (C_{13} + C_{34})}{(C_{12} + C_{24} + C_{13} + C_{34})}. \quad (B2)$$

Inserting the above values from the capacitance matrix [Eq. (B1)], we calculate $C_\Sigma \approx 2.5$ fF.

From the method of node analysis, we also derive an effective qubit-resonator coupling constant [29],

$$\beta = \frac{C_{\text{eff}}}{C_\phi} = \frac{C_{13}C_{24} - C_{12}C_{34}}{C_{23} + (C_{12} + C_{24}) \cdot (C_{13} + C_{34})}. \quad (B3)$$

The value $\beta \approx 0.24$, calculated from the capacitance matrix in Eq. (B1), indicates that the geometry displayed in Fig. 4(a) is suitable to realize strong qubit-resonator coupling $g \gg \kappa, \gamma$ with $g = (\beta e/\hbar)V_{\text{rms}}$ (κ is the cavity lifetime, γ is the qubit lifetime) [29]. Assuming a typical voltage between the coplanar resonator strips, $V_{\text{rms}} \approx 1\,\mu$eV, we obtain $g \gg 100$ MHz. In comparison with reported values for $\gamma \approx 320$ kHz [20] and $\kappa \ll 1$ MHz [40], the condition $g \gg \kappa, \gamma$ should be easily met.

APPENDIX C: EFFECTIVE GEOMETRIC CAPACITANCE OF A METALLIC TIP WIRE

The geometry of the tip, which is attached to the charge qubit (CQ) [cf. Fig. (a)], not only determines the spatial resolution, Δx, of the CQ sensor, but also its response, λ, through $\lambda \propto C_C^2$, as discussed in the main text. In the case of a nanowire tip of cylindrical shape with a flat bottom surface [Fig. 5(a)], the estimates of Δx and C_C are readily obtained through a plate capacitor model. For a tip of diameter $d = 50$ nm, separated from the sample surface by $h_0 = 1$ nm, we find $C_C \approx 2 \times 10^{-17}$ F and $\eta \approx 10^{-2}$.

In the case of a metallic tip wire, on the other hand, estimating these quantities requires to take the conical shape of the tip apex into account. Figure 5(b) displays a typical geometry of a metallic tip wire used for scanning probe operations. Previous analyses found that C_C of such a tip shape in front of a flat metallic surface can be described by [26]

$$C_C = \frac{\pi \epsilon d}{\sin(\alpha) \ln[\cot(\alpha/2)]}. \quad (C1)$$

Here, ϵ denotes the vacuum permittivity, α the opening angle of the conical tip apex, and d the tip wire diameter. A tip with $\alpha = 30°$ and $d = 5\,\mu$m will result in a geometric capacitance of $C_C \approx 0.2$ fF against a metallic sample surface and, in comparison to the nanowire tip, an enhanced $\eta \approx 10^{-1}$. Considering the attainable spatial resolution using such a metallic wire tip, it is important to appreciate that the electrostatic field is not uniformly distributed between the sample and the conical surface but is strongest near the tip apex and strongly decays with increasing distance [$\propto h(x)^{-2}$]. Hence, the effective area for the conversion of voltage noise, $\delta V(t)$, in the sample into gate charge noise, $\delta n_G(t)$, on the CQ is confined to a smaller region around the very tip apex, determining the effective spatial resolution Δx of this tip.

We estimate this effective area by calculating an effective diameter d', within which 95 % of the potential between tip and sample drops. To this end we express the tip-sample distance $h(x)$ as a function of the distance from the tip's central axis, $h(x) = \cot(\alpha)x + h_0$ (Fig. 5), and solve for the x value, which satisfies

$$0.95 \int_{h_0}^{h(d/2)} dx' \frac{1}{x'} = \int_{h_0}^{h(x)} dx' \frac{1}{x'}. \quad (C2)$$

This expression can be readily simplified and yields

$$x = \frac{2}{\cot(\alpha)} \exp[0.9 \ln(h'(d/2)) + 0.1 \ln(h_0)]. \quad (C3)$$

Assuming realistic values for metallic tip wires, $d = 5\,\mu$m and $\alpha = 30°$, we calculate an effective diameter $d' \approx 130$ nm, which determines the effective spatial resolution of SCQM using metallic tip wires.

[1] W. A. Benalcazar et al., Science **357**, 61 (2017).

[2] F. Schindler et al., Nat. Phys. **14**, 918 (2018).

[3] Y. Cao et al., Nature (London) **556**, 80 (2018).

[4] Y. Cao et al., Nature (London) **556**, 43 (2018).

[5] C. L. Degen, F. Reinhard, and P. Cappellaro, Rev. Mod. Phys. **89**, 035002 (2017).

[6] C. L. Degen, Appl. Phys. Lett. **92**, 243111 (2008).

[7] J. R. Maze et al., Nature (London) **455**, 644 (2008).

[8] G. Balasubramanian et al., Nature (London) **455**, 648 (2008).

[9] G. Kucsko et al., Nature (London) **500**, 54 (2013).

[10] A. Ariyaratne et al., Nat. Commun. **9**, 2406 (2018).

[11] D. Halbertal et al., Nature (London) **539**, 407 (2016).

[12] A. Uri *et al.*, Nature (London) **581**, 47 (2020).

[13] Y.-T. Cui *et al.*, Rev. Sci. Instrum. **87**, 063711 (2016).

[14] Y. Shi *et al.*, Sci. Adv. **5**, eaat8799 (2019).

[15] Y. Nakamura *et al.*, Nature (London) **398**, 786 (1998).

[16] Y. Nakamura, Y. A. Pashkin, T. Yamamoto, and J. S. Tsai, Phys. Rev. Lett. **88**, 047901 (2002).

[17] O. Astafiev, Y. A. Pashkin, Y. Nakamura, T. Yamamoto, and J. S. Tsai, Phys. Rev. Lett. **93**, 267007 (2004).

[18] A. Shnirman, G. Schön, I. Martin, and Y. Makhlin, Phys. Rev. Lett. **94**, 127002 (2005).

[19] D. Vion *et al.*, Science **296**, 886 (2002).

[20] D. I. Schuster, A. Wallraff, A. Blais, L. Frunzio, R.-S. Huang, J. Majer, S. M. Girvin, and R. J. Schoelkopf, Phys. Rev. Lett. **94**, 123602 (2005).

[21] J. Johnson *et al.*, Phys. Rev. **32**, 97 (1928).

[22] H. Nyquist *et al.*, Phys. Rev. **32**, 110 (1928).

[23] S. Kolkowitz *et al.*, Science **347**, 1129 (2015).

[24] A. Wallraff *et al.*, Nature (London) **431**, 162 (2004).

[25] J. Zopes, K. Sasaki, K. S. Cujia, J. M. Boss, K. Chang, T. F. Segawa, K. M. Itoh, and C. L. Degen, Phys. Rev. Lett. **119**, 260501 (2017).

[26] C. R. Ast *et al.*, Nat. Commun. **7**, 13009 (2016).

[27] W. E. Shanks *et al.*, Nat. Commun. **4**, 1991 (2013).

[28] S. Girvin *et al.*, Circuit QED: superconducting qubits coupled to microwave photons, *Quantum Machines: Measurement and Control of Engineered Quantum Systems* (Oxford University Press, Oxford, 2014), pp. 113–239.

[29] A. Blais, R. S. Huang, A. Wallraff, S. M. Girvin, and R. J. Schoelkopf, Phys. Rev. A **69**, 062320 (2004).

[30] R. Schoelkopf *et al.*, Qubits as Spectrometers of Quantum Noise, *Quantum Noise in Mesoscopic Physics* (Springer, Netherlands, 2003), pp. 175–203.

[31] U. Weiss, *Quantum Dissipative Systems* (World Scientific, Singapore, 1999).

[32] C. Macklin *et al.*, Science **350**, 307 (2015).

[33] M. H. Devoret and R. J. Schoelkopf, Science **339**, 1169 (2013).

[34] A. Nersisyan *et al.*, arXiv:1901.08042.

[35] A. P. M. Place *et al.*, arXiv:2003.00024.

[36] A. Premkumar *et al.*, arXiv:2004.02908.

[37] J. Koch, T. M. Yu, J. Gambetta, A. A. Houck, D. I. Schuster, J. Majer, A. Blais, M. H. Devoret, S. M. Girvin, and R. J. Schoelkopf, Phys. Rev. A **76**, 042319 (2007).

[38] G. Ithier *et al.*, Phys. Rev. B **72**, 134519 (2005).

[39] B. G. Christensen *et al.*, Phys. Rev. B **100**, 140503(R) (2019).

[40] J. M. Sage *et al.*, J. Appl. Phys. **109**, 063915 (2011).

[41] N. T. Bronn *et al.*, Appl. Phys. Lett. **107**, 172601 (2015).

[42] I. M. Hayes, Z. Hao, N. Maksimovic, S. K. Lewin, M. K. Chan, R. D. McDonald, B. J. Ramshaw, J. E. Moore, and J. G. Analytis, Phys. Rev. Lett. **121**, 197002 (2018).

[43] M. Assig *et al.*, Rev. Sci. Instrum. **84**, 033903 (2013).

[44] C. P. Scheller *et al.*, Appl. Phys. Lett. **104**, 211106 (2014).

[45] T. Machida *et al.*, Rev. Sci. Instrum. **89**, 093707 (2018).

[46] P. Maletinsky *et al.*, Nature Nanotech. **7**, 320 (2012).

[47] M. Leeuwenhoek *et al.*, Nanotechnology **30**, 335702 (2019).

[48] S. Geaney *et al.*, Sci. Rep. **9**, 12539 (2019).

[49] F. J. Giessibl *et al.*, Rev. Sci. Instrum. **90**, 011101 (2019).

[50] S. Montangero, T. Calarco, and R. Fazio, Phys. Rev. Lett. **99**, 170501 (2007).

[51] S. Wu *et al.*, Science **359**, 76 (2018).

[52] V. Fatemi *et al.*, Science **362**, 926 (2018).

[53] Y. Xu, Z. Song, Z. Wang, H. Weng, and X. Dai, Phys. Rev. Lett. **122**, 256402 (2019).

[54] D. A. Bandurin *et al.*, Science **351**, 1055 (2016).

[55] J. Crossno *et al.*, Science **351**, 1058 (2016).

[56] P. J. W. Moll *et al.*, Science **351**, 1061 (2016).

[57] K. Serniak, M. Hays, G. de Lange, S. Diamond, S. Shankar, L. D. Burkhart, L. Frunzio, M. Houzet, and M. H. Devoret, Phys. Rev. Lett. **121**, 157701 (2018).

[58] D. Ristè *et al.*, Nat. Commun. **4**, 1913 (2013).